Stoichiometry control and electronic and transport properties of pyrochlore $Bi_2Ir_2O_7$ thin films

W. C. Yang,[1] Y. T. Xie,[2] X. Sun,[3] X. H. Zhang,[4] K. Park,[5] S. C. Xue,[3] Y. L. Li,[5] C. G. Tao,[5] Q. X. Jia,[6] Y. Losovyj,[7] H. Wang,[3] J. J. Heremans,[5] and S. X. Zhang[1,*]

[1]*Department of Physics, Indiana University, Bloomington, Indiana 47408, USA*

[2]*SZU-NUS Collaborative Innovation Center for Optoelectronic Science & Technology, International Collaborative Laboratory of 2D Materials for Optoelectronics Science and Technology of Ministry of Education, College of Optoelectronic Engineering, Shenzhen University, Shenzhen 518060, China*

[3]*School of Materials Engineering, Purdue University, West Lafayette, Indiana 47907, USA*

[4]*Department of Physics, University of Maryland, College Park, Maryland 20742, USA*

[5]*Department of Physics, Virginia Tech, Blacksburg, Virginia 24061, USA*

[6]*Department of Materials Design and Innovation, University at Buffalo—The State University of New York, Buffalo, New York 14260, USA and Department of Physics, Konkuk University, Seoul 143-701, Korea*

[7]*Department of Chemistry, Indiana University, Bloomington, Indiana 47408, USA*

(Received 22 June 2018; revised manuscript received 2 October 2018; published 21 November 2018)

Synthesizing stoichiometric and epitaxial thin films of pyrochlore iridates is an essential step toward the experimental realization of unusual topological and magnetic states that are theoretically predicted in this unique spin-orbit coupled material system. Here, we report on the stoichiometry control and electronic and transport properties of pyrochlore iridate $Bi_2Ir_2O_7$ thin films grown by pulsed laser deposition. The as-grown films form a bilayerlike structure, in which the top surface is highly Ir deficient while the bottom layer is mainly composed of iridium metal. By postannealing the as-deposited films in $IrO_2 + O_2$ atmosphere, we improved the stoichiometry and homogeneity through the film thickness with the lattice constant close to the bulk value. Density functional theory calculation in the bulk limit shows a fourfold degenerate Dirac node slightly below the Fermi energy at the X point, along with trivial bands around the Γ point. The projected partial density of states suggests that the states in the vicinity of the Fermi energy (-3 to 0 eV) mainly consist of highly hybridized Ir $5d$ and O $2p$ with minor contributions from Bi $6s$ and $6p$, while those far below the Fermi energy (-9 to -3 eV) are contributed primarily by the O bands. Transport measurements revealed a weakly metallic behavior at higher temperatures transitioning to a weakly insulating behavior below 150 K, and a low-temperature magnetoresistance qualitatively ascribed to multicarrier and band-structural effects. The transport features are influenced by a density of states sharply peaked at the Fermi energy, and by the coexistence of trivial bands with the Dirac node, as revealed by the density functional theory calculations.

DOI: 10.1103/PhysRevMaterials.2.114206

I. INTRODUCTION

The $5d$ transition metal oxides (e.g., iridates) are correlated materials with strong spin-orbit coupling (SOC) that have attracted significant attention in recent years [1–4]. A prominent example is formed by the pyrochlore iridates $A_2Ir_2O_7$ (or A-227 with A = Bi, Y, or rare-earth element), in which exotic electronic and magnetic ground states are predicted to emerge from the interplay of electron correlation, SOC, and geometrical frustration [5–10]. The effective electron interaction is tunable by the A-site ion which has a strong influence on the local structure, in particular on the Ir-O-Ir bond angle [11]. For example, when the large Pr^{3+} ions occupy the A site, the system is in a weakly interacting regime and it forms a paramagnetic semimetal with quadratic bands touching at the Brillouin zone center [12]. By increasing the effective interaction to an intermediate regime by reducing the A-site ionic radius, the system is driven into a topological Weyl semimetal state that is accompanied by a noncollinear antiferromagnetic order [5]. Further increase of electron interaction opens up an energy gap, leading to a magnetic Mott insulator. Experimentally, the quadratic-band-touching phase has been confirmed in bulk Pr-227 crystals of weak interaction by angle-resolved photoemission spectroscopy measurement [13]; however, *direct* detection of the more exotic Weyl semimetal states in the intermediate regime remains elusive [14], although optical conductivity studies have revealed gapless features [15,16]. One speculation is that the Weyl semimetal states exist only in a very narrow window of interaction [17] which may be hard to controllably access in bulk materials.

Epitaxial thin films provide excellent opportunities to explore novel topological and magnetic states. First, the composition can be well controlled and tuned in most of the thin-film growth process, which is essential to the experimental realization of the theoretically predicted phases in real materials, especially when the access window is narrow. Second, epitaxial growth of thin films on lattice-mismatched substrates can create lattice strains in the films, or the substrate and film can deliberately be subject to controllable stress

*sxzhang@indiana.edu

 ©2018 American Physical Society

by gluing to a piezoelectric element. In both cases, strain provides another means of symmetry breaking or tunes the effective electron interaction and hence the ground states. Indeed, recent studies on thin films of the Ruddlesden-Popper iridates (e.g., Sr_2IrO_4 and $SrIrO_3$) have shown remarkable influence of elastic strains on their electronic structures and magnetic properties [18–26]. Third, pyrochlore iridate films in the ultrathin (i.e., two-dimensional) limit break the cubic symmetry and could exhibit emergent topological properties such as quantized Hall effect [17,27–30]. Finally, thin films are ideal platforms for fabricating complex device structures including heterostructures for both the fundamental study of interface physics and the realization of practical applications.

In spite of the promising features discussed above, the synthesis of pyrochlore iridate thin films has turned out to be challenging. Most of the successful growths (e.g., Eu-227 and Nd-227) so far have utilized a solid-phase epitaxy method, in which amorphous films were first deposited by pulsed laser deposition (PLD) or sputtering at a relatively low temperature and were then crystallized by postannealing at an elevated temperature [31–36]. To promote epitaxy, one must ensure that the nucleation occurs exclusively at the film-substrate interface in the annealing process. These films have shown electrical transport properties (e.g., temperature dependence of resistivity) that are notably different from those of the bulk crystals [31,34,35]. While elastic strain may play an important role on the physical properties [35], the influence of stoichiometry has not yet been ruled out [31,34]. On the other hand, epitaxial thin films of the pyrochlore iridate Bi-227 were also grown directly by PLD at a relatively high temperature [37,38]. Interesting transport characteristics including linear positive magnetoresistance and weak antilocalization were observed [37,38]. Yet, chemical compositional analysis has suggested that the films are highly Ir and oxygen deficient [38]. In this paper, we report on the stoichiometry control of epitaxial Bi-227 thin films via a postannealing approach. The as-grown films form a bilayerlike structure, in which the top surface is highly Ir deficient while the bottom layer is mainly composed of iridium metal. By postannealing the as-grown films in $IrO_2 + O_2$ atmosphere, we significantly improved the stoichiometry and homogeneity through the film thickness with the lattice constant close to the bulk value. Density functional theory (DFT) calculations on Bi-227 in the bulk limit show a fourfold degenerate Dirac node slightly below the Fermi energy E_F at the X point, in contrast to the quadratic bands touching at the Γ point in Pr-227 [12]. The DFT calculations also reveal a small sharp peak in the total density of states (DOS) at E_F, which is of importance to interpret the electronic transport measurements discussed below. The low density of carriers and concomitant reduced screening lead to a weakly metallic behavior at higher temperatures T transitioning to a weakly insulating behavior below 150 K, as revealed in transport measurements. While a chiral anomaly could not be detected, transport measurements showed a low-T magnetoresistance that could be understood in the framework of multicarrier and band-structural effects. The dependence on T and magnetic field B revealed in electronic transport reflects the influence of the coexistence of the Dirac node with trivial bands in the vicinity of E_F, and of a DOS sharply peaked at E_F, both discerned as well in the DFT calculations.

II. EXPERIMENTAL AND CALCULATION METHODS

Bi-227 thin films were deposited on yttria-stabilized zirconia (YSZ) (111) substrates using pulsed laser deposition at a laser repetition rate of 2 Hz. The PLD target was prepared through a solid-state reaction method using a mixture of IrO_2 and Bi_2O_3 at an Ir/Bi ratio of 3. Energy-dispersive x-ray spectroscopy (EDX) characterization of chemical composition was carried out in a scanning electron microscope (SEM, Quanta FEI). The EDX spectra obtained on the target show that the actual Ir/Bi ratio is ∼5.5. The KrF laser energy was set to 150, 180, and 200 mJ, corresponding to a nominal laser fluence of ∼5, 6, and 6.7 J/cm^2, respectively. The oxygen partial pressure was kept at 50 mTorr, and the substrate heater temperature was maintained at 750 °C. Postannealing of thin films was carried out in a home-built three-zone quartz-tube furnace. IrO_2 powder was placed in zone 2, and the Bi-227 thin film was in zone 3. High-purity oxygen gas flowed from zone 2 to zone 3 at a flow rate of 50 sccm. The oxygen pressure was kept at 300 Torr during the annealing process. Zone 2 was first heated to 1000 °C at a ramp rate of 50 °C/min, after which the temperature of zone 3 was increased to ∼500 °C at 50 °C/min. The two zones were then maintained at the soak temperatures for 0.5 h, after which the furnace was naturally cooled down to room temperature.

X-ray diffraction (XRD) measurements were performed using either a Bruker D8 DISCOVER diffractometer or a PANalytical Empyrean diffractometer, where the Cu $K\alpha$ line was selected as the incident beam. The 2θ-ω spectra were collected by a scintillation detector, and the reciprocal space mapping (RSM) scans were measured using a position-sensitive detector (Vantec). The RSM data were analyzed and plotted using PYTHON. The cross-sectional samples for transmission electron microscopy (TEM) analysis were prepared via mechanical grinding, dimpling, and a low-energy ion polishing step (PIPS 691, Gatan, Inc.). The TEM, scanning transmission electron microscopy (STEM), and electron-dispersive x-ray spectroscopy (EDX) analysis were conducted using a FEI TALOS F200X at 200 kV, equipped with ultrahigh-resolution high-angle annular dark field detectors, and super-X EDX. Scanning tunneling microscopy (STM) characterizations were carried out in an ultrahigh-vacuum STM (Omicron) system with a base pressure of 5.5×10^{-10} Torr at room temperature. The STM tip was chemically etched tungsten. The Bi-227 sample was annealed at 200 °C at the same base pressure for 3 h before STM measurements. Atomic force microscopy (AFM) measurements were carried out on a Dimension Icon (Bruker Corporation) instrument. ScanAsyst-Air cantilevers (NCST, NanoWorld) with a spring constant of 0.4 N/m, normal resonance frequencies 70 kHz, and nominal tip radius of 2 nm were employed in ScanAsyst-Air mode. X-ray photoelectron spectroscopy (XPS) was carried out using a PHI (Physical Electronics) VersaProbe II instrument equipped with a focused monochromatic Al $K\alpha$ source [38–40]. Magnetotransport measurements were performed on a microfabricated L-shaped Hall bar mesa, fabricated by photolithography followed by reactive ion etching in BCl_3 (Supplemental

Material, Fig. S1 [41]). The L shape allowed the characterization of anisotropic transport properties. The active region of the Hall bar featured a length of 160 μm and a width of 80 μm. Magnetotransport data were obtained over 1.3 K $< T <$ 297 K in systems allowing different orientation of B with respect to the film plane. Excitation currents varied between 1 μA and 1 mA, depending on measurement temperature.

DFT calculations were performed on Bi-227 in the pyrochlore structure (space group 227, Fd-3m), by using VASP [42,43]. The generalized gradient approximation [44] and projector-augmented wave pseudopotentials [45] were employed, and the spin-orbit coupling was included self-consistently within DFT formalism. For the calculation of band structure and density of states (DOS), we considered a face-centered cubic primitive unit cell consisting of 22 atoms with the experimental lattice constant of 10.311 Å [46], and used an energy cutoff of 400 eV and 9 × 9 × 1 k-point mesh. The structure was found to not carry any net magnetization.

III. RESULTS AND DISCUSSION

The Bi-227 thin films obtained using a laser fluence of ~5 J/cm^2 were epitaxially grown on the YSZ (111) substrate but showed significant off-stoichiometry. As shown in Fig. 1(a), only the (111) family of film peaks were observed in the XRD θ-2θ scan, indicating a (111)-oriented growth. A fine scan exhibits clear oscillations around the (222) peak of the thin film [inset of Fig. 1(a)], revealing high crystalline quality and smooth surface. The out-of-plane lattice constants d_{222} of these as-grown films were calculated to be 3.01–3.02 Å, about 1% larger than that of the bulk samples (~2.98 Å) [46,47]. This out-of-plane elongation is ascribed to both off-stoichiometry and in-plane compression of the thin films. Indeed, our EDX characterization suggests a low Ir/Bi ratio of 0.55–0.65 in the as-grown films. Since Bi^{3+} has a larger ionic radius than Ir^{4+} [48], the replacement of Ir by Bi can result in an overall lattice expansion. Furthermore, as the lattice constant of Bi-227 is larger than that of the YSZ substrate, an in-plane compressive strain (and hence out-of-plane elongation) is expected as a result of epitaxial growth, which is confirmed via reciprocal space mapping of the [202] peak. As depicted in Fig. 1(b), the film peak lies below the full relaxation line of the cubic structure, indicating that the in-plane lattice of the thin film (along the x direction) is indeed compressed while the out-of-plane lattice (along the z direction) is elongated. In comparison to the films grown using a lower laser fluence of ~3.3 J/cm^2 [38], both the Ir/Bi ratio and the out-of-plane lattice constant in this work are closer to the bulk values. Further increase of laser fluence reduces the lattice constant and increases the Ir/Bi ratio (Supplemental Material, Fig. S2 [41]). Yet, XRD θ-2θ measurement shows Ir metal peaks in the films grown with a high laser fluence of ~6 and ~6.7 J/cm^2. Therefore, the following discussions will focus on the films grown at a laser fluence of ~5 J/cm^2 unless otherwise noted.

A typical cross-sectional high-resolution (HR) TEM image [Fig. 2(a)] of the film-substrate interface area exhibits clear lattice fringes in the film, suggesting high crystallinity of the sample. The corresponding selected-area electron diffraction (ED) pattern [Fig. 2(b)] reveals well-distinguished

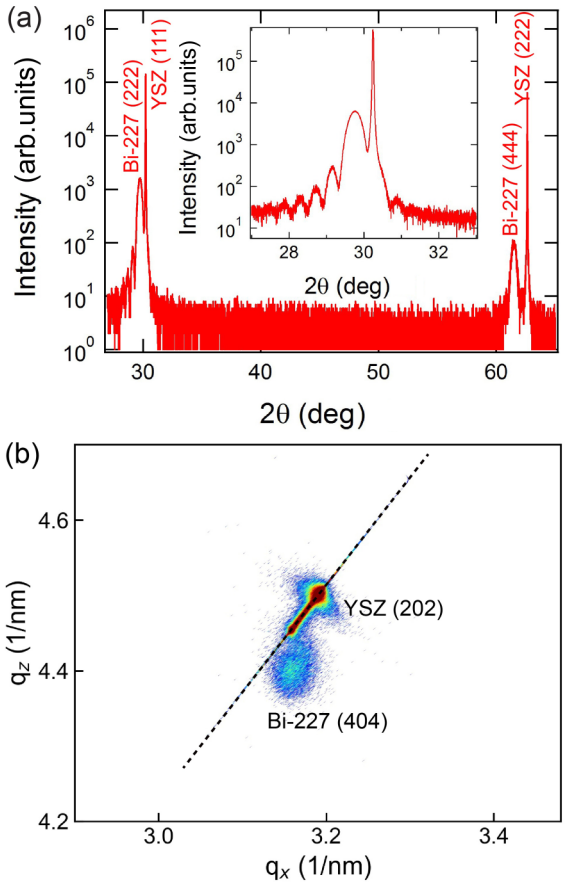

FIG. 1. (a) X-ray diffraction θ-2θ scan of a Bi-227 thin film grown on YSZ (111) using a laser fluence of ~5 J/cm^2. The inset shows a fine scan around the (222) peak of the film. (b) Reciprocal space mapping around the YSZ (202) peak. The intensity was normalized and plotted in log scale. The dashed line extrapolates to the origin of the q_x-q_z graph and hence represents a full relaxation of the cubic structure.

diffraction dots similar to the ones from the substrate [Fig. 2(c)], confirming the high epitaxial quality of the film on the substrate. The epitaxial relationships of the film and the substrate are determined to be (222)Bi-227‖(111)YSZ and [02$\bar{2}$]Bi-227||[01$\bar{1}$]YSZ. The matched lattice fringes and high-quality epitaxial growth are also evidenced in the high-resolution STEM image in Fig. 2(d). It is noted that the HR TEM image [Fig. 2(a)] shows a thin dark layer near the film-substrate interface suggesting the growth of a thin disordered layer at the early stage of deposition. Such disordered interface region is also obvious in the STEM image [Fig. 2(d)]), revealed as a bright contrast layer, indicating a higher average atomic number Z. The EDX mapping in Fig. 2(g) suggests that the interface layer (~2.5 nm) is highly Ir rich, while the bulk part of the film appears more uniform. The interface layer also has minimal Bi and O signals [Figs. 2(f) and 2(h)], indicating the formation of a metal Ir layer. It is worth noting that Ir nanocrystals were also observed in Nd-227 thin films grown by solid-state epitaxy [33]. The absence of obvious Ir peaks in the XRD θ-2θ measurement [Fig. 1(a)] suggests that the Ir metal layer is very thin and may have very fine grain size.

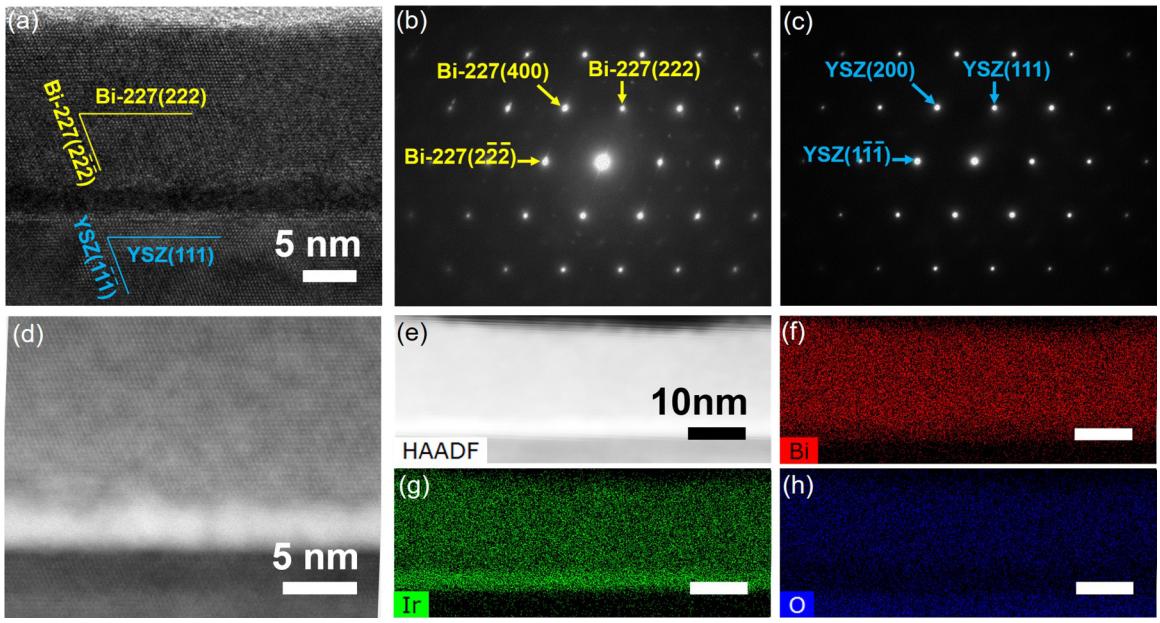

FIG. 2. (a) Cross-sectional TEM image of a Bi-227 film grown on YSZ (111) substrate. Selected-area electron diffraction pattern taken from (b) the thin film and (c) the YSZ substrate region. (d) High-resolution STEM image showing clear lattice fringes of the film and the substrate. (e) STEM image of the thin film and the corresponding EDX mapping of the elements of (f) Bi, (g) Ir, and (h) O.

A postannealing approach was developed to realize high-quality and stoichiometric thin films. Figure 3(a) depicts a schematic illustrating the annealing process: IrO_2 powder was first heated up to 1000 °C at which it sublimated to form vapor; the flow of oxygen gas carried the iridium oxide vapor downstream to react with the as-grown thin film at ∼500 °C for 0.5 h. As shown in Fig. 3(b) and its inset, the film maintains its (111) preferential orientation, and the (222) and (444) peaks shift to higher angles after annealing, indicating that the out-of-plane lattice constant is reduced. The value of d_{222} calculated using the (444) peak is 2.99 Å, only ∼0.3% larger than the bulk value [46,47]. We note that misfit dislocation and strain relaxation may give rise to a change of lattice constant. To check if this is the case upon annealing, we did reciprocal space mapping of an annealed sample. As shown in Fig. 3(c), the annealed film is still under compressive in-plane strain, similar to the as-grown films [Fig. 1(b)]. The change in lattice constant is associated with the improved stoichiometry of the film after annealing. Indeed, EDX characterization at two different spots on an annealed film shows an Ir/Bi ratio of 1.0 ± 0.2 and 1.0 ± 0.3 (Supplemental Material, Fig. S3 [41]), confirming the expected cation stoichiometry within the experimental uncertainties. The major uncertainty in the EDX is likely due to the large background signal from the bulk substrate that is underneath the film. We therefore carried out more surface-sensitive x-ray photoelectron spectroscopy (XPS) measurements on an annealed film; the Ir/Bi ratio determined from the XPS spectra was 1.038 ± 0.004 (Supplemental Material, Fig. S4 [41]), which further confirms the stoichiometry of the films. The surface morphology of an annealed film was characterized by STM, and it shows a local overall surface roughness (root mean square height) of about 1.18 nm (Supplemental Material, Fig. S5 [41]), which is comparable to that of the Eu-227 films grown by solid-state epitaxy [31]. High crystalline quality of the annealed films is further confirmed by cross-sectional TEM [Fig. 4]. As shown in Fig. 4(b), lattice fringes are clearly seen in both the film and the substrate. The EDX mapping of the cross-sectional image in Figs. 4(d)–4(f) shows a more uniform distribution of elements than in the as-grown film [Figs. 2(f)–2(h)], and the Ir sublayer was essentially diminished.

Our previous DFT calculation suggests that the point defects in the Ir-deficient films are antisite Bi_{Ir} rather than Ir vacancies [38]. These high-density antisite defects were eliminated by postannealing in $IrO_2 + O_2$ vapor, resulting in a decrease of lattice constant (again, since Ir^{4+} has a smaller ionic radius than Bi^{3+} [48]). The annealing contains three major processes: (1) creation of highly volatile IrO_3, (2) transport of IrO_3 gas phase toward the film, and (3) chemical reaction between IrO_3 and the Ir-deficient film. According to previous studies [49], the following chemical reaction, $2IrO_2(s) + O_2(g) = 2IrO_3(g)$, occurs in the first process where the temperature is below 1100 °C. The equilibrium constant for this reaction is $K_p = \frac{(P_{IrO3})^2}{P_{O2}}$, where P_{IrO3} and P_{O2} are the partial pressure of IrO_3 and O_2. Cordfunke *et al.* determined a temperature-dependent equilibrium constant: $\log K_p = -\frac{27\,596}{T} + 16.902$ [49]. We therefore calculated the partial pressure of IrO_3 to be $P_{IrO3} = 0.07$ Torr based on $T = 1000\,^{\circ}C$ (or 1273 K) and $P_{O2} = 300$ Torr. In the second process, the IrO_3 gas is transported by the carrier gas toward the thin film placed downstream in the quartz-tube reactor [Fig. 3(a)]. In the third process, the IrO_3 (g) reacts with the Ir-deficient thin film, and the Ir atoms replace the Bi_{Ir} antisite defects, leaving excess Bi in the vapor phase. Based on the standard Gibbs energy equations for the formation of gaseous bismuth and bismuth oxides [50], we found that Bi_4O_6 (g) is the most stable phase among a variety of bismuth vapor species at the annealing temperature of 500 °C (or 773 K). Given that the Ir metal sublayer near the substrate interface

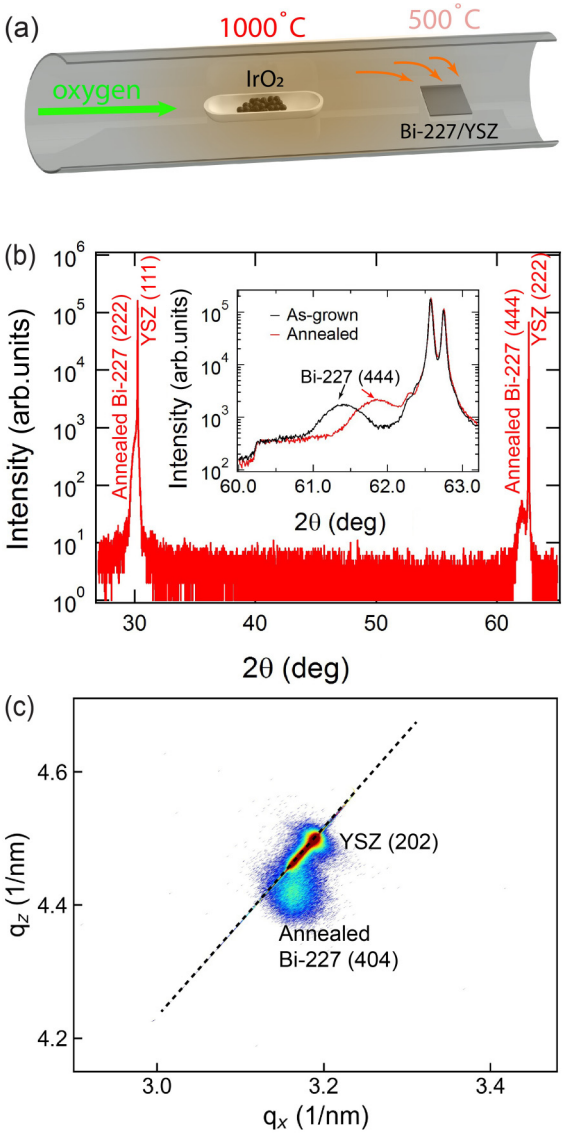

FIG. 3. (a) A schematic picture showing the annealing process. (b) XRD θ-2θ scan of an annealed sample; the inset shows fine scans around the (444) peak of the films taken using a PANalytical Empyrean diffractometer. The two patterns were calibrated using the YSZ substrate peak, and their intensities were normalized for a better comparison of the film peak positions. (c) Reciprocal space mapping around the YSZ (202) peaks. The intensity was normalized and plotted in log scale. The dashed line extrapolates to the origin of the q_x-q_z graph and hence represents a full relaxation of the cubic structure.

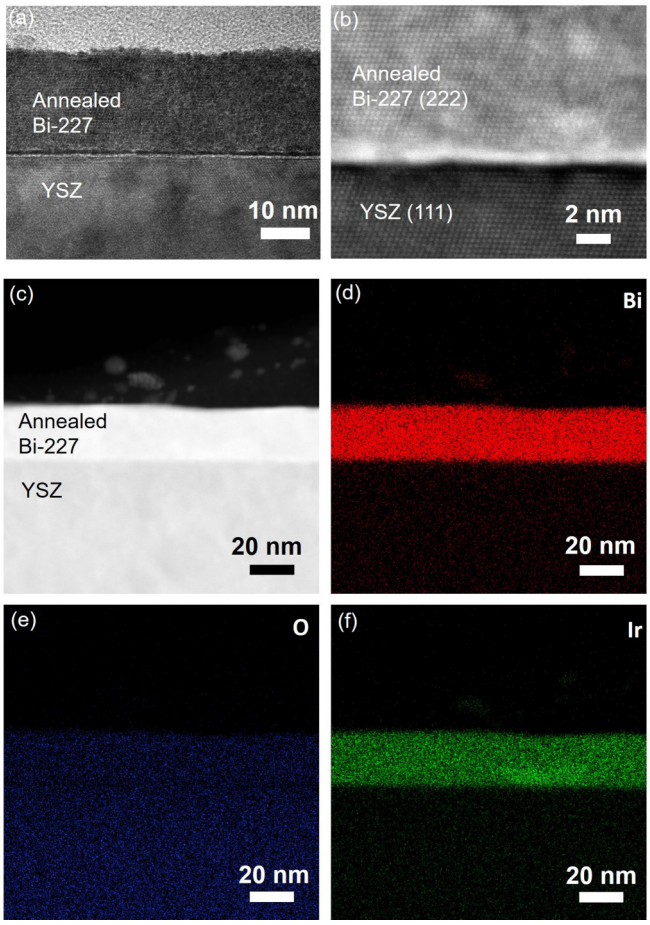

FIG. 4. (a) Cross-sectional TEM image, (b) scanning TEM, and EDX mapping of (d) Bi, (e) O, and (f) Ir of an annealed Bi-227 thin film. A slight variation of thickness was observed in different sample regions.

was significantly diminished after annealing, it is reasonable to believe that the Ir atoms in the metal layer also diffuse into the bulk of the film and replace the Bi_{Ir} antisite defects. It is worth noting that although postannealing is involved in both the solid-state epitaxy [31–35] and our approach here, the mechanisms differ: In the former case, the annealing crystallizes an amorphous film, utilizing the single-crystalline nature of the substrate as a driving force for epitaxy; in the latter (i.e., our case), the annealing tunes the stoichiometry of an as-grown, epitaxial film, without altering its crystal structure. By controlling the annealing atmosphere, one can essentially apply our approach to other binary or ternary material systems that consist of elements with highly distinct vapor pressures, to achieve stoichiometry.

The electronic properties of the Bi-227 films were studied by DFT calculations. It is noted that most of the previous theoretical studies of electronic properties were focused on ultrathin films that are composed of only a few trigonal/kagome atomic layers [27–30]. Since the films in this work are about 20 nm thick, which corresponds to ~66 atomic layers, here we carried out calculations in the three-dimensional bulk limit. Given the large ionic radius of Bi^{3+}, the electron interaction is believed to be rather weak and the Hubbard U term (on-site Coulomb repulsion) was hence set to zero. As observed in Figs. 5(a) and 5(b), the electronic structure shows a fourfold degenerate Dirac node at 57 meV below E_F at the X point. This Dirac semimetallic feature is similar to that in β-cristobalite BiO_2, which has the same space group and was suggested to be a nonsymmorphic Dirac semimetal with a fourfold degenerate Dirac node at the X point at E_F [51]. The linear dispersion is in contrast to the quadratic band touching in another metallic pyrochlore iridate, namely, Pr-227 in which the effective electron

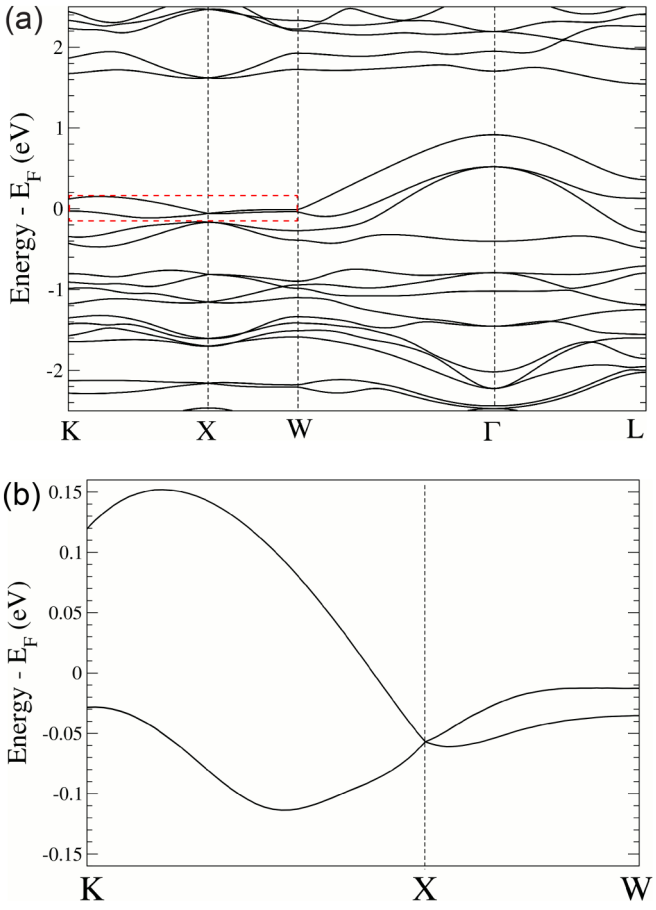

FIG. 5. (a) Electronic band structure of Bi-227 calculated using DFT, where energies are referred relative to the Fermi energy E_F. (b) Electronic band structure zoomed in near the Dirac node at the X point [as denoted by the box in (a)].

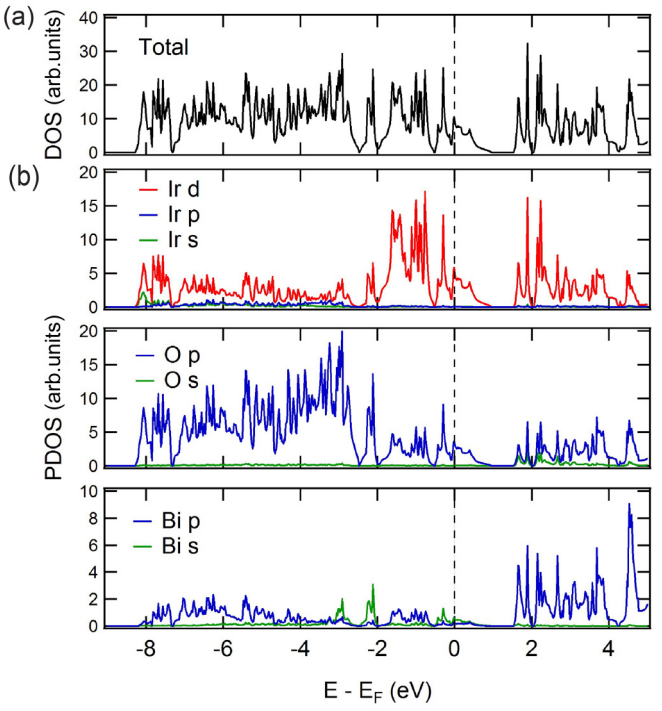

FIG. 6. (a) Total density of states and (b) projected partial density of states onto the orbitals for Bi-227 calculated using DFT. Energies are referred relative to E_F (dashed lines).

interaction is also considered to be weak due to the large radius of Pr^{3+}. Coexisting with the Dirac nodes in Bi-227 are some trivial bands around the Γ point [Fig. 5(a)].

The total DOS in Fig. 6(a) exhibits a small sharp peak at E_F, qualitatively consistent with previous calculations [46]. As a result, the electrical properties are anticipated to be sensitive to perturbations that can shift E_F away from the local maximum in the total DOS. The projected partial DOS shown in Fig. 6(b) suggests that the states in the vicinity of E_F (−3 to 0 eV) mainly consist of Ir $5d$ and O $2p$ along with some minor contributions from Bi $6s$ and $6p$, while those far below E_F (−9 to −3 eV) are contributed primarily by the O bands. The large overlap of the occupied states as well as their unoccupied counterpart (above E_F) suggests strong hybridization between these orbitals.

Finally, we studied the electronic transport properties of the annealed film, and we link the observed transport properties to the DFT calculations. The dependence on T of the sheet resistance (two-dimensional resistivity) $R_\square$ at $B = 0$ and the low-T magnetoresistance [(MR), $R_\square$ *vs* B] were obtained on an L-shaped Hall bar mesa (Supplemental Material, Fig. S1 [41]) prepared by photolithography and dry etching. The L-shaped Hall bar, aligned along perpendicular and nonequivalent crystal directions [22$\bar{4}$]Bi-227 and [2$\bar{2}$0]Bi-227, additionally allows the detection of anisotropic carrier transport properties, since a study of transport anisotropy has not received much attention in the pyrochlores. The sample displayed anisotropy, with values for $R_\square$ at $B = 0$ and $T = 4.2$ K of approximately 2750 Ω/□ in the high-resistivity direction [22$\bar{4}$]Bi-227 ($R_\square \to R_{xx}$) and 1300 Ω/□ in the low-resistivity direction [2$\bar{2}$0]Bi-227 ($R_\square \to R_{yy}$). This stoichiometric film also displayed a sensitivity to cooldown protocol, leading to a variation in measured values for $R_\square$ of about 7%. The sensitivity is attributed to E_F lying at a small but sharp peak in the DOS, as inferred from the DFT calculations. A small variation in E_F can then lead to susbstantial variation in DOS at E_F, to which transport properties are sensitive.

The main panel in Fig. 7(a) depicts $R_\square = R_{xx}$ vs T for 4.2 K $< T <$ 297 K obtained in the high-resistivity direction [22$\bar{4}$]Bi-227 at $B = 0$. A weakly metallic behavior at high T transitions to a weakly insulating behavior for $T <$ 150 K. The changeover and resulting minimum in $R_\square$ vs T is not believed to be due to an electronic or structural transition. The weakly insulating behavior results only in a maximal ∼6% increase in sheet resistance between 150 and 4.2 K, and is hence not as pronounced as the insulating behavior that would result from a band gap. The data [Fig. 7(a) and its inset for $B = 0$] further do not closely fit a power law $R_\square \sim T^{-\alpha}$, in contrast to observations in bulk single crystals [46] and further do not follow $1/R_\square \sim \ln(T)$, as would be expected from the Aronov-Altshuler mechanism for electron-electron interactions [52–54] due to an effective suppression of the DOS at E_F. The broad minimum in sheet resistance at 150 K and the weakly insulating behavior for $T <$ 150 K are instead ascribed to the competition between decreasing scattering of

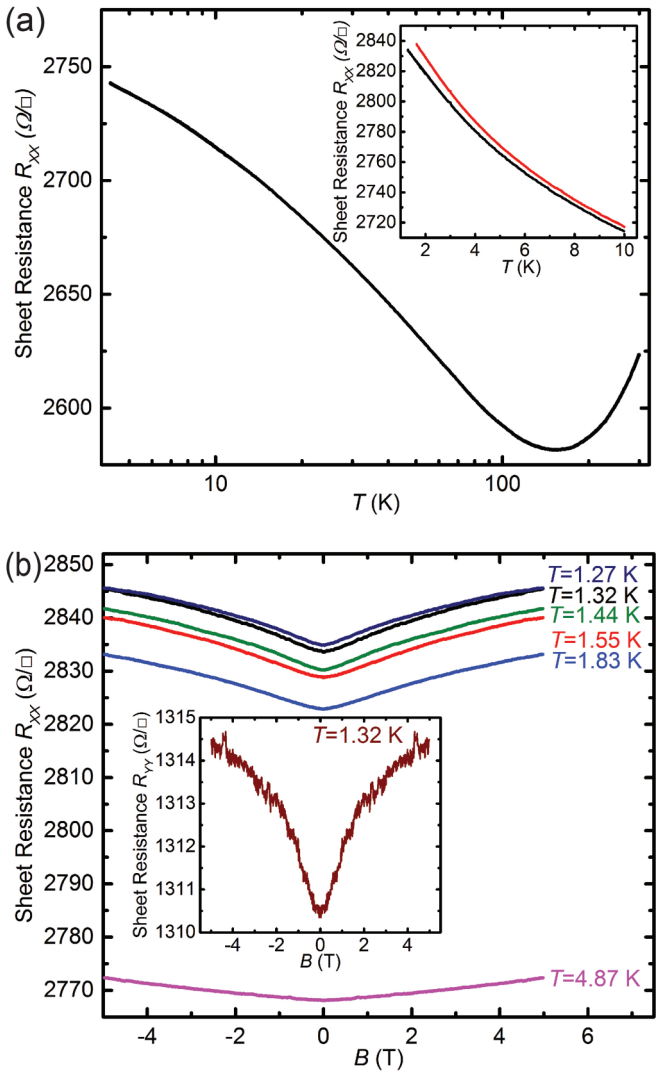

FIG. 7. (a) Sheet resistance $R_\square$ vs T at $B = 0$ in the high-resistivity direction [22$\bar{4}$]Bi-227 ($R_\square = R_{xx}$). The inset shows $R_\square = R_{xx}$ vs T under $B = 0$ (black curve) and under $B = 5\,\mathrm{T}$ applied perpendicularly to the film surface (red curve) in the high-resistivity direction [22$\bar{4}$]Bi-227, for 1.3 K $< T <$ 10 K. Due to the sensitivity to cooldown protocol, a slight variation in sheet resistance (a few percent) is noted at the same T for different traces. (b) Magnetoresistance $R_\square = R_{xx}$ vs B at indicated T in the high-resistivity direction [22$\bar{4}$]Bi-227. The traces are obtained under different field conditions as explained in the text. The inset shows the magnetoresistance $R_\square = R_{yy}$ vs B at 1.32 K in the low-resistivity direction [2$\bar{2}$0]Bi-227, after cooldown to ∼1.30 K at $B = 0$.

carriers by phonons with decreasing T, and a progressive carrier trapping at lower T, in a disorder potential largely unscreened due to a relatively low DOS at E_F. These findings are supported by the DFT calculations. Strain in the film can also contibute to disorder, to which transport properties will be sensitive, although not necessarily detectable in TEM studies. The observed transport anisotropy along [22$\bar{4}$]Bi-227 compared to [2$\bar{2}$0]Bi-227 would not be expected for unstrained bulk crystals with cubic symmetry. Nevertheless, a transport anisotropy is regularly observed in thin films of cubic crystals. The anisotropy has not received as much attention in pyrochlores as it has in technologically important face-centered cubic semiconductors such as multivalley Si [55,56] and Ge [57–61] or high-index GaAs [62], where the anisotropy is well recognized and taken into account in device fabrication. The anisotropy in Si, Ge, and GaAs has been attributed to effects on band-structure carrier valleys of residual strain (resulting in an effectively uniaxial distortion) and surface effects breaking the cubic symmetry [55,58,60], and to anisotropic scattering (i.e., surface scattering, phonon scattering, intervalley scattering, or impurity scattering not conforming to the cubic symmetry) [56,57,59,61,62]. In the multivalley semiconductors the exact origin of the experimentally observed anisotropy has typically not been straightforward to discern, and likewise, the origin of the observed transport anisotropy between [22$\bar{4}$]Bi-227 and [2$\bar{2}$0]Bi-227, while an experimental fact, has not been elucidated. In the present work, STM on the Bi-227 thin film (cf. Supplemental Material, Fig. S5 [41]) and AFM on the YSZ substrate (cf. Supplemental Material, Fig. S6 [41]) did not detect surface morphologies (e.g., ripples) that could induce anisotropic surface or interface scattering [57,62]. Possibly, the predominantly biaxial strain originating in the film growth on YSZ substrates [as evidenced by the RSM data in Fig. 3(c)] has a residual uniaxial component breaking the cubic symmetry and contributing to the anisotropy. Anisotropic phonon scattering, intervalley scattering, or impurity scattering cannot be excluded. Further, Fig. S7 of the Supplemental Material [41] (calculated by DFT) is included to show the multivalley character of the Bi-227 around E_F [41], and the figure highlights the different energy dispersions found in the valleys along the [22$\bar{4}$]Bi-227 and [2$\bar{2}$0]Bi-227 directions. As in Si and Ge, the multivalley character likely renders Bi-227 prone to transport anisotropy due to the mechanisms enumerated above. The inset in Fig. 7(a) compares $R_\square = R_{xx}$ vs T for 1.3 K $< T <$ 10 K, in the high-resistivity direction [22$\bar{4}$]Bi-227 for cooldowns at $B = 0$ and at $B = 5\,\mathrm{T}$ (with B applied perpendicularly to the film surface). While MR is evident from the comparison, no evidence for a magnetic transition [63] is apparent in the range 1.3 K $< T <$ 10 K.

Figure 7(b) contains measurements of MR ($R_\square = R_{xx}$ over -5 T $< B <$ 5 T) in the high-resistivity direction [22$\bar{4}$]Bi-227 at different T. The traces at 4.87, 1.83, 1.55, and 1.32 K were obtained with B applied perpendicularly to the film surface, after cooldown under $B = 0$. The trace at $T = 1.44\,\mathrm{K}$ was obtained with B applied perpendicularly to the film but after cooling the sample from 10 K under perpendicular $B = 5\,\mathrm{T}$. The trace at $T = 1.27\,\mathrm{K}$ was obtained (after $B = 0$ cooldown) with B applied in plane and parallel to the measurement current direction, hence parallel to the electric field over the sample, to probe the presence of possible chiral anomaly, potentially induced by lifting of the degeneracy of the Dirac node (not observed, cf. below). Magnetic hysteresis in the MR traces could not be observed in any of the cases, pointing to an absence of magnetic order. The gradual evolution under decreasing T apparent from the comparison of the traces obtained at 4.87, 1.83, 1.55, and 1.32 K also argues for the absence of a magnetic transition in this range of T, as corroborated by the data in the inset of Fig. 7(a). The Aronov-Altshuler mechanism for electron-electron interactions [52–54] is not favored by the dependence

of $R_\square$ on T at $B = 0$ [Fig. 7(a)] and is thereby eliminated as a source of the observed positive MR. Instead, the positive MR and its gradual dependence on T [Fig. 7(a) inset] may indicate the existence of multiple types of charge carriers, originating in the presence of multiple bands in the electronic structure (Fig. 5 and Ref. [64]). The complex band structure as calculated by DFT (Fig. 5), featuring a coexistence of the Dirac node with trivial bands in the vicinity of E_F, supports the contribution of multiple types of charge carriers. The MR at $T = 4.87$ K assumes a more pronounced linear dependence on B at higher B. A linear positive MR at high B can be due to a linear or quasirelativistic dispersion of the underlying electronic structure (as observed in topological insulators, Bi, Dirac materials, and narrow-gap semiconductors) [65]. In the present material, the linear dispersion characteristic of the Dirac node just below E_F can contribute to the linear MR. While a detailed analysis is not emphasized in the present work, the observed MR hence appears to result from a combination of several phenomena, including multicarrier effects and linear MR due to band structure, both features supported by the DFT calculations. It is also noted that the MR obtained with B applied parallel to the electric field over the sample ($T = 1.27$ K) does not substantially differ from the MR obtained under perpendicular B, and hence effects of a chiral anomaly [66] cannot be inferred. The inset of Fig. 7(b) depicts the MR ($R_\square = R_{yy}$ vs B) in the low-resistivity direction [$2\bar{2}0$]Bi-227, obtained at $T = 1.32$ K. This MR bears a strong resemblance to the MR obtained in the high-resistivity direction at 1.32 K, but is of somewhat lower relative magnitude (3% rather than 4% over 5 T). Comparing the present thin-film results for $R_\square$ vs T [Fig. 7(a)] with results on a bulk $Bi_2Ir_2O_7$ sample [46], we find that the metallic low-T dependence $R_\square \sim T^{3/2}$ observed in the bulk sample for $1.7\ \text{K} < T < 10$ K is not observed in the thin film, while Ref. [46] similarly concludes that the sensitivity of transport properties to external parameters can originate in E_F lying at a small but sharp peak in the DOS. Concerning $R_\square$ vs B [Fig. 7(b)], the bulk $Bi_2Ir_2O_7$ sample [46] lacks significant MR for $B \leqslant 14$ T, in contrast to the present thin-film material.

IV. CONCLUSIONS

In summary, we developed a postannealing approach to tune the stoichiometry and lattice parameters of Bi-227 thin films grown by pulsed laser deposition. The as-grown films form a bilayerlike structure, in which the top layer is highly Ir-deficient Bi-227 while the bottom layer is mainly composed of Ir metal. By postannealing in $IrO_2 + O_2$ atmosphere, we significantly improved the stoichiometry and homogeneity through the film thickness with the lattice constant close to the bulk value. The same approach may be applied to other nonstoichiometric binary or ternary material systems to control stoichiometry. DFT calculations in the bulk limit show a fourfold degenerate Dirac node slightly below the Fermi energy at the X point, coexisting with trivial bands around the Γ point. The projected partial DOS suggests that the states in the vicinity of the Fermi energy (-3 to 0 eV) mainly consist of highly hybridized Ir $5d$ and O $2p$ with minor contributions from Bi $6s$ and $6p$. The states further below the Fermi energy (-9 to -3 eV) are contributed mainly by the O bands. Transport measurements could not detect a chiral anomaly, but showed a weakly metallic behavior at higher temperatures transitioning to a weakly insulating behavior below 150 K. Transport measurements also showed a low-temperature magnetoresistance, attributed to multicarrier and band-structural effects.

ACKNOWLEDGMENTS

S.X.Z. acknowledges Indiana University (IU) College of Arts and Sciences for startup support. H.W. and X.S. acknowledge the support from the U.S. National Science Foundation (Grant No. DMR-1565822) for the TEM/STEM effort at Purdue University. J.J.H. and Y.T.X. were supported by the U.S. Department of Energy, Office of Basic Energy Sciences, Division of Materials Sciences and Engineering under Award No. DOE DE-FG02-08ER46532. The authors also acknowledge the Nanoscale Characterization Facility for the use of the SEM and XPS instruments and the Indiana University Molecular Structure Center for XRD facility (NSF Grant No. 400 CHE-1048613).

[1] W. Witczak-Krempa, G. Chen, and Y. B. Kim, Annu. Rev. Condens. Matter Phys. **5**, 57 (2013).
[2] R. Schaffer, E. K. H. Lee, B. J. Yang, and Y. B. Kim, Rep. Prog. Phys. **79**, 094504 (2016).
[3] J. G. Rau, E. K. H. Lee, and H. Y. Kee, Annu. Rev. Condens. Matter Phys. **7**, 195 (2016).
[4] G. Cao and P. Schlottmann, Rep. Prog. Phys. **81**, 042502 (2018).
[5] X. G. Wan, A. M. Turner, A. Vishwanath, and S. Y. Savrasov, Phys. Rev. B **83**, 205101 (2011).
[6] D. Pesin and L. Balents, Nat. Phys. **6**, 376 (2010).
[7] K. Y. Yang, Y. M. Lu, and Y. Ran, Phys. Rev. B **84**, 075129 (2011).
[8] W. Witczak-Krempa and Y. B. Kim, Phys. Rev. B **85**, 045124 (2012).
[9] M. Kargarian, J. Wen, and G. A. Fiete, Phys. Rev. B **83**, 165112 (2011).
[10] Y. Machida, S. Nakatsuji, S. Onoda, T. Tayama, and T. Sakakibara, Nature **463**, 210 (2010).
[11] H. J. Koo, M. H. Whangbo, and B. J. Kennedy, J. Solid State Chem. **136**, 269 (1998).
[12] E. G. Moon, C. K. Xu, Y. B. Kim, and L. Balents, Phys. Rev. Lett. **111**, 206401 (2013).
[13] T. Kondo, M. Nakayama, R. Chen, J. J. Ishikawa, E. G. Moon, T. Yamamoto, Y. Ota, W. Malaeb, H. Kanai, Y. Nakashima, Y. Ishida, R. Yoshida, H. Yamamoto, M. Matsunami, S. Kimura, N. Inami, K. Ono, H. Kumigashira, S. Nakatsuji, L. Balents *et al.*, Nat. Commun. **6**, 10042 (2015).
[14] M. Nakayama, T. Kondo, Z. Tian, J. J. Ishikawa, M. Halim, C. Bareille, W. Malaeb, K. Kuroda, T. Tomita, S. Ideta, K. Tanaka, M. Matsunami, S. Kimura, N. Inami, K. Ono, H. Kumigashira, L. Balents, S. Nakatsuji, and S. Shin, Phys. Rev. Lett. **117**, 056403 (2016).

[15] K. Ueda, J. Fujioka, Y. Takahashi, T. Suzuki, S. Ishiwata, Y. Taguchi, and Y. Tokura, Phys. Rev. Lett. **109**, 136402 (2012).

[16] A. B. Sushkov, J. B. Hofmann, G. S. Jenkins, J. Ishikawa, S. Nakatsuji, S. Das Sarma, and H. D. Drew, Phys. Rev. B **92**, 241108(R) (2015).

[17] K. Hwang and Y. B. Kim, Sci. Rep. **6**, 30017 (2016).

[18] C. Rayan Serrao, J. Liu, J. T. Heron, G. Singh-Bhalla, A. Yadav, S. J. Suresha, R. J. Paull, D. Yi, J.-H. Chu, M. Trassin, A. Vishwanath, E. Arenholz, C. Frontera, J. Železný, T. Jungwirth, X. Marti, and R. Ramesh, Phys. Rev. B **87**, 085121 (2013).

[19] J. Nichols, J. Terzic, E. G. Bittle, O. B. Korneta, L. E. De Long, J. W. Brill, G. Cao, and S. S. A. Seo, Appl. Phys. Lett. **102**, 141908 (2013).

[20] J. Nichols, O. B. Korneta, J. Terzic, L. E. De Long, G. Cao, J. W. Brill, and S. S. A. Seo, Appl. Phys. Lett. **103**, 131910 (2013).

[21] L. D. Miao, H. Xu, and Z. Q. Mao, Phys. Rev. B **89**, 035109 (2014).

[22] A. Lupascu, J. P. Clancy, H. Gretarsson, Z. X. Nie, J. Nichols, J. Terzic, G. Cao, S. S. A. Seo, Z. Islam, M. H. Upton, J. Kim, D. Casa, T. Gog, A. H. Said, V. M. Katukuri, H. Stoll, L. Hozoi, J. van den Brink, and Y. J. Kim, Phys. Rev. Lett. **112**, 147201 (2014).

[23] N. Domingo, L. Lopez-Mir, M. Paradinas, V. Holy, J. Zelezny, D. Yi, S. J. Suresha, J. Liu, C. R. Serrao, R. Ramesh, C. Ocal, X. Marti, and G. Catalan, Nanoscale **7**, 3453 (2015).

[24] L. Y. Zhang, Q. F. Liang, Y. Xiong, B. B. Zhang, L. Gao, H. D. Li, Y. B. Chen, J. Zhou, S. T. Zhang, Z. B. Gu, S. H. Yao, Z. M. Wang, Y. Lin, and Y. F. Chen, Phys. Rev. B **91**, 035110 (2015).

[25] B. Kim, B. H. Kim, K. Kim, and B. I. Min, Sci. Rep. **6**, 27095 (2016).

[26] X. R. Liu, Y. W. Cao, B. Pal, S. Middey, M. Kareev, Y. Choi, P. Shafer, D. Haskel, E. Arenholz, and J. Chakhalian, Phys. Rev. Mater. **1**, 075004 (2017).

[27] B. J. Yang and N. Nagaosa, Phys. Rev. Lett. **112**, 246402 (2014).

[28] X. Hu, A. Rüegg, and G. A. Fiete, Phys. Rev. B **86**, 235141 (2012).

[29] X. Hu, Z. C. Zhong, and G. A. Fiete, Sci. Rep. **5**, 11072 (2015).

[30] Q. Chen, H. H. Hung, X. Hu, and G. A. Fiete, Phys. Rev. B **92**, 085145 (2015).

[31] T. C. Fujita, Y. Kozuka, M. Uchida, A. Tsukazaki, T. Arima, and M. Kawasaki, Sci. Rep. **5**, 9711 (2015).

[32] T. C. Fujita, M. Uchida, Y. Kozuka, W. Sano, A. Tsukazaki, T. Arima, and M. Kawasaki, Phys. Rev. B **93**, 064419 (2016).

[33] J. C. Gallagher, B. D. Esser, R. Morrow, S. R. Dunsiger, R. E. A. Williams, P. M. Woodward, D. W. McComb, and F. Y. Yang, Sci. Rep. **6**, 22282 (2016).

[34] Y. Kozuka, T. C. Fujita, M. Uchida, T. Nojima, A. Tsukazaki, J. Matsuno, T. Arima, and M. Kawasaki, Phys. Rev. B **96**, 224417 (2017).

[35] T. Ohtsuki, Z. Tian, A. Endo, M. Halim, S. Katsumoto, Y. Kohama, K. Kindo, S. Nakatsuji, and M. Lippmaa, arXiv:1711.07813.

[36] T. C. Fujita, Y. Kozuka, J. Matsuno, M. Uchida, A. Tsukazaki, T. Arima, and M. Kawasaki, Phys. Rev. Mater. **2**, 011402(R) (2018).

[37] J.-H. Chu, S. C. Riggs, M. Shapiro, J. Liu, C. R. Serero, D. Yi, M. Melissa, S. J. Suresha, C. Frontera, A. Vishwanath, X. Marti, I. R. Fisher, and R. Ramesh, arXiv:1309.4750v2.

[38] W. C. Yang, Y. T. Xie, W. K. Zhu, K. Park, A. P. Chen, Y. Losovyj, Z. Li, H. M. Liu, M. Starr, J. A. Acosta, C. G. Tao, N. Li, Q. X. Jia, J. J. Heremans, and S. X. Zhang, Sci. Rep. **7**, 7740 (2017).

[39] Z. Li, E. Z. Xu, Y. Losovyj, N. Li, A. P. Chen, B. Swartzentruber, N. Sinitsyn, J. Yoo, Q. X. Jia, and S. X. Zhang, Nanoscale **9**, 13014 (2017).

[40] E. Z. Xu, H. M. Liu, K. Park, Z. Li, Y. Losovyj, M. Starr, M. Werbianskyj, H. A. Fertig, and S. X. Zhang, Nanoscale **9**, 3576 (2017).

[41] See Supplemental Material at http://link.aps.org/supplemental/10.1103/PhysRevMaterials.2.114206 for Hall device fabrication and geometry; influence of laser fluence on film composition and lattice constant; EDX, XPS, and STM characterizations of thin films; AFM characterization of YSZ substrate; density-functional-theory calculation of the electronic band structure.

[42] G. Kresse and J. Furthmuller, Phys. Rev. B **54**, 11169 (1996).

[43] G. Kresse and J. Furthmuller, Comput. Mater. Sci. **6**, 15 (1996).

[44] J. P. Perdew, K. Burke, and M. Ernzerhof, Phys. Rev. Lett. **77**, 3865 (1996).

[45] P. E. Blochl, Phys. Rev. B **50**, 17953 (1994).

[46] T. F. Qi, O. B. Korneta, X. Wan, L. E. DeLong, P. Schlottmann, and G. Cao, J. Phys.: Condens. Matter **24**, 345601 (2012).

[47] Y. S. Lee, S. J. Moon, S. C. Riggs, M. C. Shapiro, I. R. Fisher, B. W. Fulfer, J. Y. Chan, A. F. Kemper, and D. N. Basov, Phys. Rev. B **87**, 195143 (2013).

[48] R. D. Shannon, Acta Crystallogr., Sect. A **32**, 751 (1976).

[49] E. H. P. Cordfunke and G. Meyer, Recl. Trav. Chim. Pays-Bas **81**, 495 (1962).

[50] S. C. Marschman and D. C. Lynch, Can. J. Chem. Eng. **62**, 875 (1984).

[51] S. M. Young, S. Zaheer, J. C. Y. Teo, C. L. Kane, E. J. Mele, and A. M. Rappe, Phys. Rev. Lett. **108**, 140405 (2012).

[52] P. A. Lee and T. V. Ramakrishnan, Rev. Mod. Phys. **57**, 287 (1985).

[53] R. S. Markiewicz and C. J. Rollins, Phys. Rev. B **29**, 735 (1984).

[54] B. L. Altshuler and A. G. Aronov, Solid State Commun. **30**, 115 (1979).

[55] R. F. Pierret and C. T. Sah, Solid State Electron. **11**, 279 (1968).

[56] M. V. Fischetti, Z. Ren, P. M. Solomon, M. Yang, and K. Rim, J. Appl. Phys. **94**, 1079 (2003).

[57] A. H. A. Hassan, R. J. H. Morris, O. A. Mironov, R. Beanland, D. Walker, S. Huband, A. Dobbie, M. Myronov, and D. R. Leadley, Appl. Phys. Lett. **104**, 132108 (2014).

[58] Y. I. Gorkun, V. S. Lysenko, V. G. Litovchenko, and V. A. Novominskii, Phys. Status Solidi A **3**, K281 (1970).

[59] C. Morrison and M. Myronov, Appl. Phys. Lett. **111**, 192103 (2017).

[60] S. Dissanayake, Y. Zhao, S. Sugahara, M. Takenaka, and S. Takagi, J. Appl. Phys. **109**, 033709 (2011).

[61] V. Aubry-Fortuna and P. Dollfus, J. Appl. Phys. **108**, 123706 (2010).

[62] J. J. Heremans, M. B. Santos, K. Hirakawa, and M. Shayegan, J. Appl. Phys. **76**, 1980 (1994).

[63] P. J. Baker, J. S. Möller, F. L. Pratt, W. Hayes, S. J. Blundell, T. Lancaster, T. F. Qi, and G. Cao, Phys. Rev. B **87**, 180409(R) (2013).

[64] Q. Wang, Y. Cao, X. G. Wan, J. D. Denlinger, T. F. Qi, O. B. Korneta, G. Cao, and D. S. Dessau, J. Phys.: Condens. Matter **27**, 015502 (2015).

[65] M. Veldhorst, M. Snelder, M. Hoek, C. G. Molenaar, D. P. Leusink, A. A. Golubov, H. Hilgenkamp, and A. Brinkman, Phys. Status Solidi RRL **7**, 26 (2013).

[66] E. Barnes, J. J. Heremans, and D. Minic, Phys. Rev. Lett. **117**, 217204 (2016).

Supplemental Material for

Stoichiometry control, electronic and transport properties of pyrochlore $Bi_2Ir_2O_7$ thin films

W. C. Yang[1], Y. T. Xie[2], X. Sun[3], X. H. Zhang[4], K. Park,[5], S. C. Xue[3], Y. L. Li[5], C. G. Tao[5], Q.X. Jia[6,7], Y. Losovyj[8], H. Wang[3], J. J. Heremans[5], and S. X. Zhang[1]*

1. Department of Physics, Indiana University, Bloomington, IN 47408, USA

2. SZU-NUS Collaborative Innovation Center for Optoelectronic Science & Technology, International Collaborative Laboratory of 2D Materials for Optoelectronics Science and Technology of Ministry of Education, College of Optoelectronic Engineering, Shenzhen University, Shenzhen 518060, China

3. School of Materials Engineering, Purdue University, West Lafayette, IN 47907, USA

4. Department of Physics, University of Maryland, College Park, MD 20742, USA

5. Department of Physics, Virginia Tech, Blacksburg, VA 24061, USA

6. Department of Materials Design and Innovation, University at Buffalo – The State University of New York, Buffalo, NY 14260, USA

7. Department of Physics, Konkuk University, Seoul 143-701, Korea

8. Department of Chemistry, Indiana University, Bloomington, IN 47408, USA

* sxzhang@indiana.edu

1. Hall device fabrication and geometry

Magnetotransport studies were performed on an L-shaped Hall bar mesa (Fig. S1), microfabricated on the thin film material by photolithography and reactive ion etching in BCl_3. The two arms of the L-shape were aligned with the non-equivalent crystal directions $[22\bar{4}]$ and $[2\bar{2}0]$ of Bi-227 and thereby allowed a characterization of the transport anisotropy. Orientations and dimensions are indicated in Fig. S1.

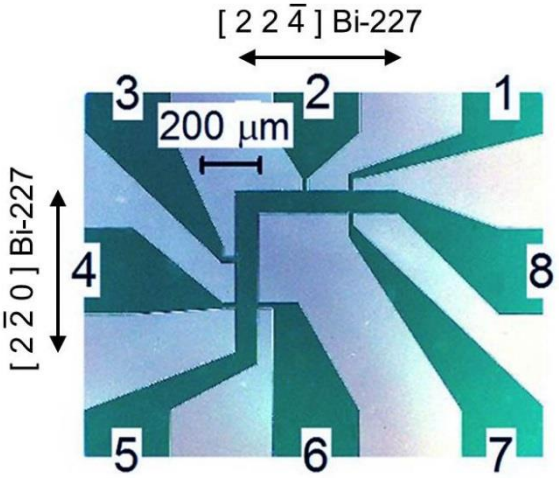

Fig. S1. Top view of the microfabricated L-shaped Hall bar mesa for the magnetotransport measurements, with Bi-227 crystal directions and dimensions indicated. The actual Hall bar mesa is indicated by the darker regions, while from the lighter regions the thin film Bi-227 is removed down to the substrate by etching. The measurement current is applied between contacts labeled "5" and "8", while other contacts are used to measure the resulting voltages.

2. Influence of laser fluence on film composition and lattice constant

Fig. S2 shows the laser fluence dependence of Ir/Bi ratio and lattice constant. The Ir/Bi ratios were measured using energy-dispersive X-ray spectroscopy, and the lattice constants were determined by X-ray diffraction. With the increase of fluence, the Ir/Bi ratio increases while the lattice constant d_{444} decreases.

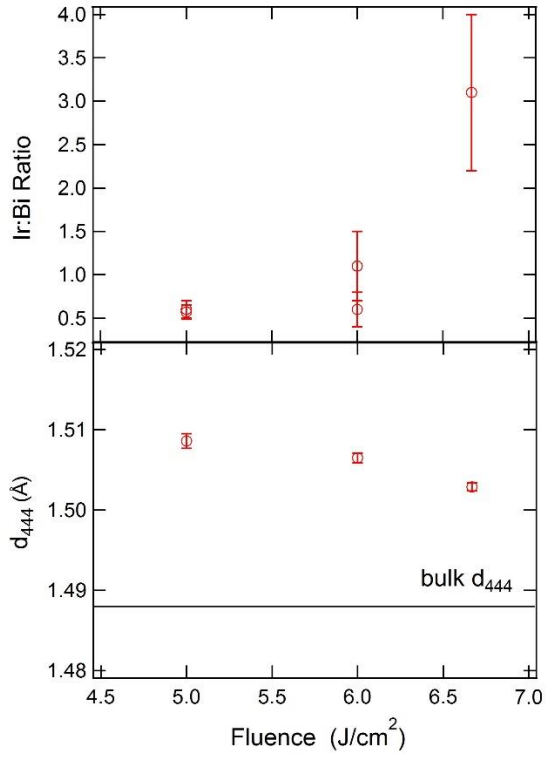

Fig. S2. The Ir/Bi ratio and d_{444} (Å) versus the nominal laser fluence (J/cm^2).

3. Energy-dispersive X-ray (EDX) spectroscopy study of annealed thin film

EDX was employed to characterize the chemical composition of thin films. Figure S3 (a) and (b) are the EDX spectra taken from two different spots of one post-annealed thin film, which confirms the existence of Ir and Bi in the film and determines the stoichiometry of the film. The Y, Zr and Hf signals are from the YSZ substrate which often contains Hf impurity. The atomic ratio of Ir/Bi was calculated based on the atomic and weight percentages obtained in the AZtech software. The ratio is determined to be 1.0±0.2 and 1.0±0.3 at the two spots.

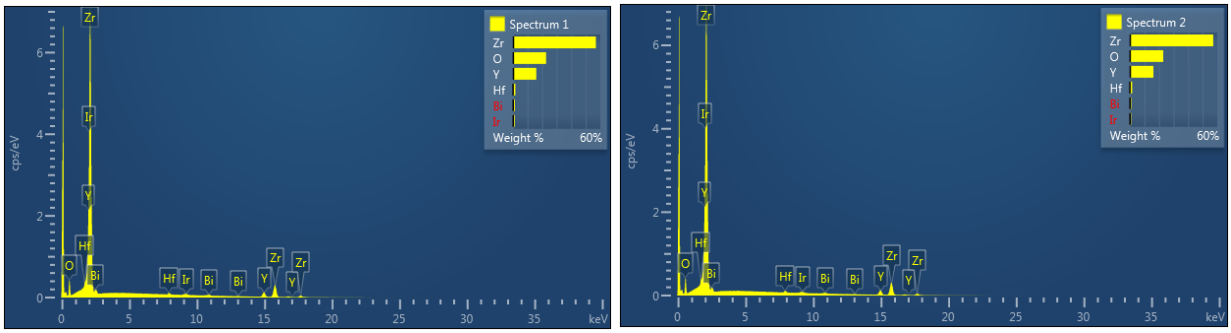

Fig. S3. (a) EDX spectrum taken from one spot, the Ir% and Bi% is 0.29% (1±13.6%) and 0.28% (1±15.3%) respectively (b) EDX spectrum taken from another spot, the Ir% and Bi% is 0.22% (1±18.8%) and 0.23% (1±19.3%) respectively.

4. X-ray photoelectron spectroscopy (XPS) measurement of annealed thin film

The XPS measurement was carried out at three different spots of an annealed thin film. Fig. S4 shows the Bi and Ir spectra, based on which we determined the Ir : Bi ratio using MultiPak software. The Ir : Bi ratio is calculated to be 1.038 ± 0.004, consistent with the EDX result.

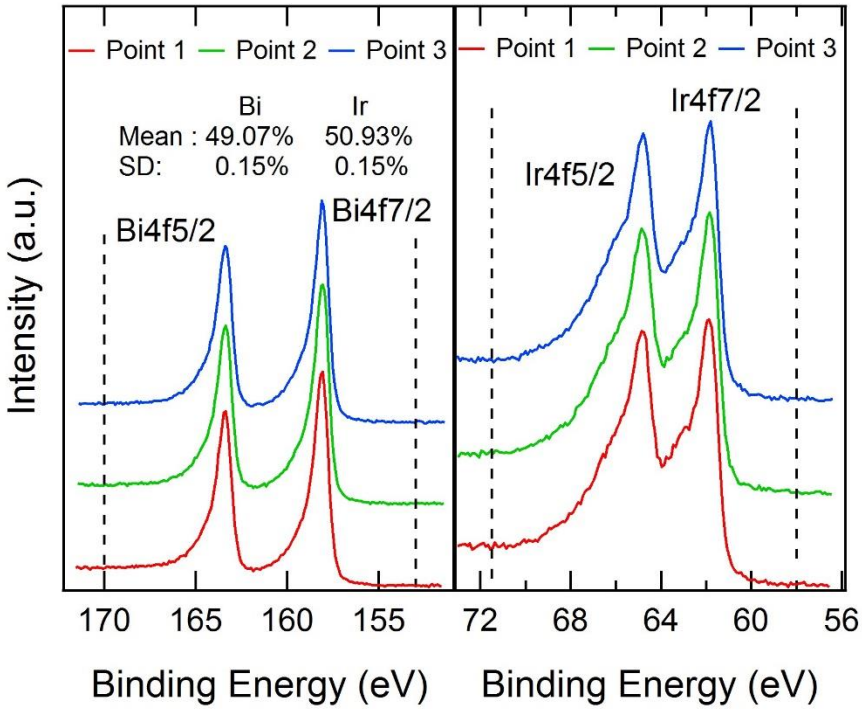

Fig. S4. Spectra of Bi and Ir taken on three different spots on an annealed thin film. The spectra are vertically shifted for clarity. The dashed lines denote the range of binding energy included for atomic% determination. The average atomic% of Bi and Ir are determined to be 49.07% and 50.93% with an uncertainty (standard deviation) of 0.15%.

5. Scanning tunneling microscopy (STM) study of surface morphology of thin film

STM was employed to characterize the surface morphology of thin film. Fig. S5 (a) is a typical large scale STM image of the annealed Bi-227 surface. The overall surface roughness (root mean square height) is about 1.18 nm. Fig. S5 (b) is a zoomed in image of the area marked by the blue square in (a), showing a much smoother morphology with a roughness of 0.21 nm.

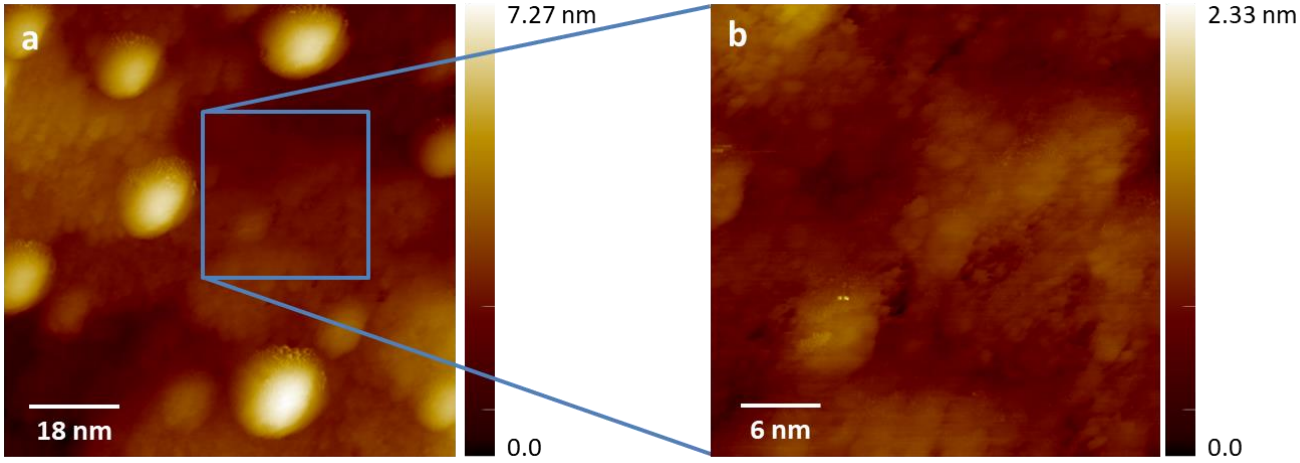

Fig. S5. (a) Typical STM image of $Bi_2Ir_2O_7$ surface (V_s = 1.60 V, I = 0.15 nA). (b) A small scale STM image of the area marked by the blue square in (a) (V_s = 1.60 V, I = 0.15 nA).

6. Atomic force microscopy (AFM) characterization of surface morphology of the YSZ substrate

AFM measurement was performed to characterize the surface morphology of an insulating YSZ substrate. As shown in Fig. S6, the single crystal YSZ substrate has a rather smooth surface without detectable step terraces or ripples.

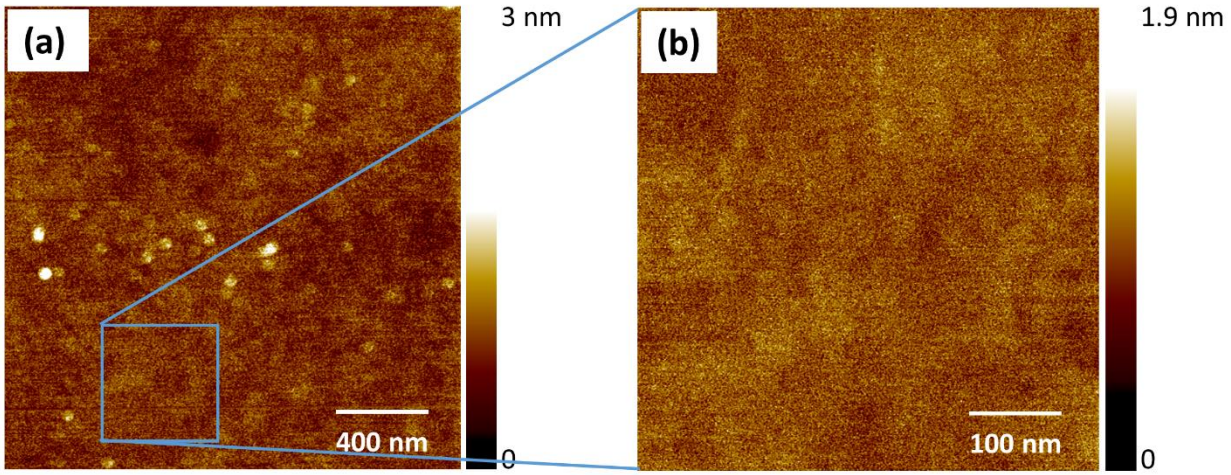

Fig. S6. Atomic force microscopy images taken on a blank YSZ substrate

7. Density-functional-theory calculation of the electronic bandstructure

Density Functional Theory (DFT) calculations were performed on Bi-227 in the pyrochlore structure, as described in the main text. The DFT calculations are integral to the work, enabling, among other findings, the discussion of the electronic transport properties. Figure S7 depicts the DFT-calculated bandstructure along the two different directions $[22\bar{4}]$Bi-227 and $[2\bar{2}0]$Bi-227, along which measurements for the film sheet resistances $R_{\square}$ were carried out (Fig. S1). In magnetotransport an anisotropic $R_{\square}$ is apparent, yielding values at B = 0 and T = 4.2 K of approximately 2750 Ω/□ in the high-resistivity direction $[22\bar{4}]$Bi-227 ($R_{\square} = R_{xx}$) and 1300 Ω/□ in the low resistivity direction $[2\bar{2}0]$Bi-227 ($R_{\square} = R_{yy}$). In Fig. S7, the calculated Fermi energy E_F for the nominally undoped material is indicated as a horizontal, dashed line. The carrier pockets defining the Fermi surface are apparent from Fig. S7. The calculation for the undoped material with the position of E_F as indicated in Fig. S7 *e.g.* predicts two carrier pockets close to the zone boundary in the low resistivity direction $[2\bar{2}0]$Bi-227, and one carrier pocket close to the zone boundary in high-resistivity direction $[22\bar{4}]$Bi-227.

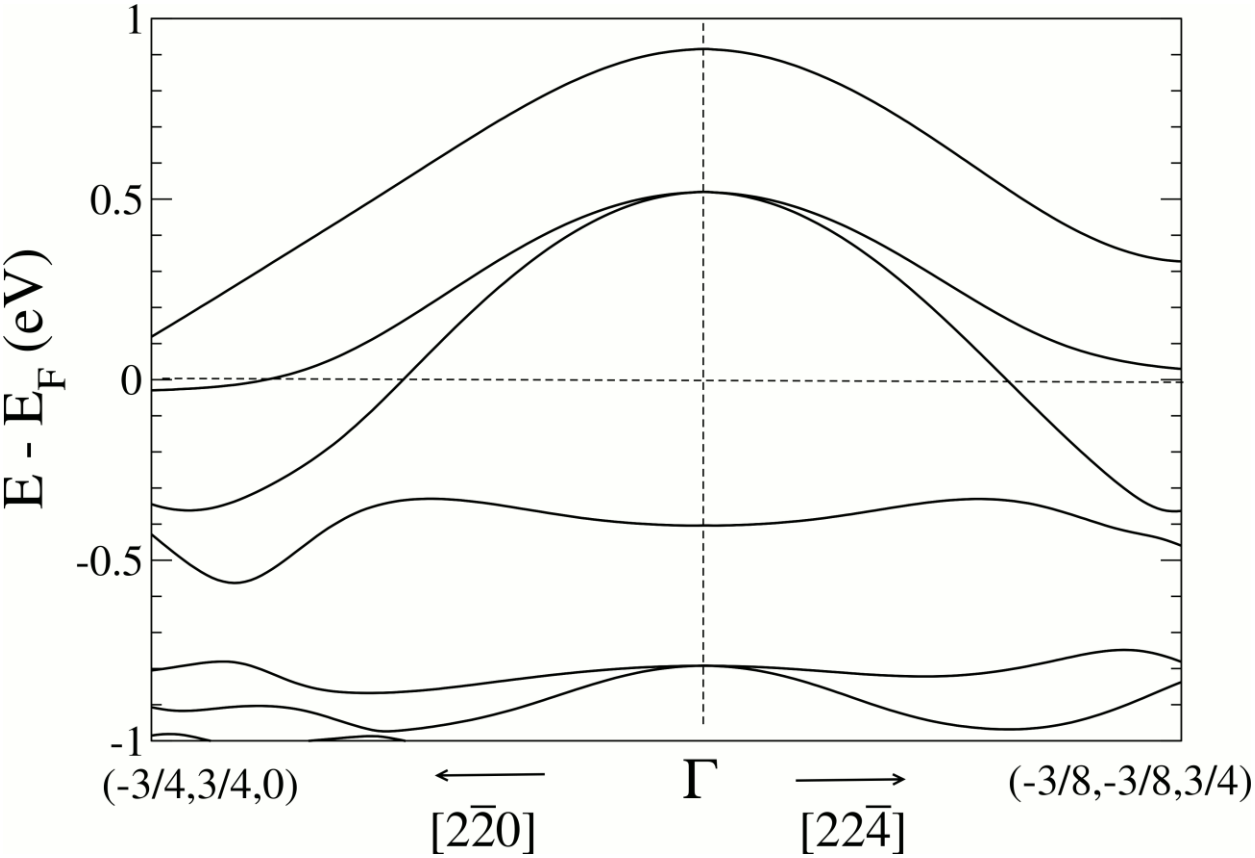

Fig. S7. DFT-calculated bandstructure along the two different directions, [22$\bar{4}$]Bi-227 and [2$\bar{2}$0]Bi-227, parallel to which magnetotransport measurement were carried out. Energies are referred relative to E_F, itself indicated as a dashed line. The points at the zone boundary along the two different directions are indicated in Cartesian coordinates in units of $2\pi/a$, where a denotes the lattice constant, 10.311 Å.